Data-Driven Transient Stability Evaluation of Electric Distribution Networks Dominated by EV Supercharging Stations

Jimiao Zhang, *Member*, and Jie Li, *Member*, *IEEE*

***Abstract*—Accelerated deployment of high-power electric vehicle (EV) supercharging stations is expected to alleviate EV drivers' range anxiety, while imposing stress on the electric distribution networks (EDNs) and threatening their transient stability. As a powerful transient stability evaluation (TSE) tool, the estimation of region of attraction (ROA) plays a vital role in maintaining situational awareness and stable operation of the emerging EDNs. However, EDNs dominated by EV charging stations typically involve highly nonlinear and complex system dynamics, rendering the model-based approaches for ROA estimation computationally intensive. Thus, solution accuracy is usually compromised due to simplified system modeling. This paper proposes a data-driven approach to ROA estimation of emerging EDNs based on the Koopman operator theory. Numerically stable Koopman eigenfunctions can be learned from the system measured data and then employed to establish a set of linearly parameterized Lyapunov candidate functions. Various trajectory data are then employed to establish a tight feasible polytope. Through efficient sampling and linear optimization, the union of invariant sublevel sets of the determined Lyapunov functions can constitute a tight inner approximation to the actual ROA. The proposed method is evaluated to be computationally efficient and permits real-time ROA estimation. Numerical simulations of a DC EDN interfaced to an AC grid validate the superior performance of the proposed method.**

***Index Terms*—Data-driven, EV charging, Koopman operator, region of attraction, transient stability evaluation.**

I. Introduction

Globally, transportation is one of the major contributors to greenhouse gas (GHG) emissions. In the United States, the transportation sector is responsible for 28% of the GHG emissions and has even overtaken the electric power sector as the nation's largest source of GHG emissions in 2020 [1]. Electric vehicles (EVs), which can run on electricity from renewable energy sources such as solar photovoltaic (PV) and wind without direct tailpipe emissions, are regarded as a game changer for the transition to a carbon-neutral transportation sector, as well as for the improvement of air quality and public health. Government initiatives, such as New Jersey's ambitious goal of registering 330,000 EVs by 2025 [2], coupled with emerging high-power charging technologies [3], are accelerating the adoption of EVs. However, the rapid buildout of EV supercharging stations will place a substantial strain on existing electric distribution networks (EDNs). The EVs, tightly regulated by power converters, behave as constant power loads (CPLs) of the EDNs with negative impedance characteristics [4], thereby reducing the system's effective damping. Moreover, a rising penetration of power-converter-interfaced renewables, commonly paired with EV charging, could lower system inertia and increase system dynamics' volatility. This could severely threaten the transient stability of emerging EDNs, undermining their ability to maintain the system frequency and voltage within the acceptable ranges following significant disturbances. Hence, it is crucial to develop efficient transient stability evaluation (TSE) approaches for ensuring system situational awareness and stable EDN operation.

There has been a growing body of research on TSE of electric power systems (EPSs) [5,6]. These works mainly utilize Lyapunov's stability theory to quantify how large disturbances a system can tolerate via the estimation of region of attraction (ROA) of a locally asymptotically stable equilibrium point [7]. Takagi-Sugeno (T-S) multi-modeling approach, originally developed for system identification [8], has been utilized for ROA estimation of various EPSs [9,10], including a multi-bus inverter-based dynamic microgrid that accounted for communication latencies [11]. As system complexity and nonlinearity increase, the T-S method struggles with high-dimensional problems despite its effectiveness for small-scale EPSs. While model reduction techniques such as Kron reduction [12] can be used to reduce computational burdens, they run the risk of omitting important system dynamics. In addition, Brayton-Moser's mixed potential theory has been applied to simplify EPSs as RLC networks for ROA estimation, where stability is guaranteed if the mixed potential function is at a local minimum [13]. This simplification, however, tends to generate conservative ROA estimates. To combat this issue, a revised mixed potential theory was introduced [14] that takes into account the operating limits of practical CPLs in DC microgrids and differentiates the state variables according to their strong and weak correlations to stability.

Among the Lyapunov-based methods, mathematical optimization, especially sum-of-squares programming (SOSP), has been extensively leveraged to compute the maximum ROA from a proper Lyapunov function [15]. This type of method carries the potential to systematically construct Lyapunov

Jimiao Zhang and Jie Li are with the Electrical and Computer Engineering Department, Rowan University, Glassboro, NJ 08028, USA, (e-mails: zhangj@rowan.edu, lijie@rowan.edu).

functions and is more accurate than other mainstream Lyapunov-based approaches. Nonetheless, SOSP is generally limited to polynomial systems. For non-polynomial system models, Taylor series expansions need to be employed at the expense of truncation errors. To counter the negative effects of truncation errors on the estimated ROA, [16] integrated bounded uncertain terms to the Taylor expansion of the trigonometric function in the original EPS models. The transient stability of grid-connected converters with phase-locked loops (PLLs) was studied in [17] using an iterative SOSP method. However, the discussed system only consisted of a single converter. It is thus unclear if the proposed method would be computationally efficient for an EDN dominated by distributed assets such as EV charging stations and renewables. Realizing that, conventional SOSP-based methods may encounter computational complexity, particularly with higher-order polynomial Lyapunov functions or in large-scale systems. To this end, reference [18] proposed a method to estimate high quality ROAs for a DC microgrid with CPLs, based on the variants of conventional SOSP with improved solution times and scalability.

The crux of Lyapunov-based research is the lack of a method for finding a generalized Lyapunov function for different systems. As an alternative, geometric methods such as normal form analysis have also been applied to ROA estimation [19]. However, these geometry tools are constrained by their locality and low dimensionality [20]. Besides, authors of [21] applied the theory of occupation measures to approximate the ROA of EPSs comprising synchronous generators (SGs). Nevertheless, the method's suitability relies heavily on polynomial reformulation of the original dynamical system models.

All the model-based methods discussed above have only investigated homogenous bus dynamics, focusing on either power converters or SGs, both of which are essential components of emerging EDNs with distinct dynamics. Besides, these methods' performances are often constrained by their system modeling accuracy, which is often compromised due to simplified mathematical models in exchange for acceptable solution times. However, practical EDNs exhibit high nonlinearity and complex dynamics, introduced by uncertainties due to varying operating conditions, as well as stochastic EV charging behavior and intermittent renewable generation. Moreover, proprietary and undisclosed control algorithms for distributed assets could exacerbate these uncertainties. Meanwhile, recent advancements in data-driven approaches, fostered by the integration of big data and advanced analytics, have led to the increased application of the Koopman operator-based methods in dynamical system analysis [22]. The Koopman operator theory allows for a scalable reconstruction of the underlying dynamical system using only measured data and provides a principled linear embedding of nonlinear dynamics, thereby reducing computational complexities. Indeed, the prominent features of the Koopman operator theory have lent itself to a wide range of data-driven applications in EPSs. such as dynamic state estimation [23], power flow calculations [24], system identification [25], model predictive control (MPC) of wind farms [26], etc. Most notably, this theory finds its application in TSE due to its ability to capture system stability properties via spectral properties and eigenfunctions [27]. However, existing research employing the Arnoldi-type method to approximate the Koopman operator failed to capture system nonlinearity adequately [28,29]. Furthermore, the spectral analysis results are generally posterior, thus reducing their comprehensibility and directness compared with ROA visualization. Reference [30] proposed an ROA estimation scheme using the extended dynamic mode decomposition (EDMD) method [31]. However, it lacks rigorous theoretical stability guarantees, and EDMD's single-time-step approximation may result in instability and accumulated approximation errors in the learned Koopman operator [32].

To address the challenges of uncertainties in emerging EDNs with enormous growth of EV supercharging stations, this work presents a novel data-driven approach using the Koopman operator theory for ROA estimation. Specifically, this method employs data regression to approximate Koopman eigenfunctions, which then facilitates the ROA estimation by constructing specially designed Lyapunov candidate functions. This proposal offers a distinct advantage over existing model-based methods by greatly improving both solution accuracy and computational performance. The major contributions of this paper are summarized as follows:

1. A tight inner approximation to the ROA of an EDN with heterogeneous bus dynamics is efficiently computed using measured data. Convex constraints are rigorously enforced on the measured trajectory data of the EDN to obtain a tight feasible polytope. Therefore, sublevel sets of the corresponding Lyapunov functions are found via sampling and linear programming (LP) to derive the estimation of ROA.

2. A set of linearly parameterized Lyapunov candidate functions are designed using the approximated Koopman eigenfunctions. This novel design not only reduces the number of decision variables in ROA estimation with improved computational efficiency, compared with optimization-based methods (e.g., SOSP), but also is directly interpretable from the perspective of Koopman spectral analysis and stability properties.

3. To overcome the instability issues inherent in the EDMD, a stable Koopman operator is learned by imposing stability constraints using the data-driven SOC algorithm [33,34]. The longer-term (multiple time steps) accuracy of the approximated Koopman eigenfunctions is improved as well.

The remainder of this paper is organized as follows: Section II describes the detailed dynamical modeling of a typical DC EDN for future EV supercharging stations, with individual distributed assets modeled separately. In Section III, the preliminaries of the Koopman operator theory are firstly presented, the issue of divergent accumulated approximation errors due to the unstable Koopman operator learned by the EDMD is analyzed, and then the SOC algorithm is introduced to overcome this issue to learn a stable Koopman operator. In Section IV, the data-driven ROA estimation method based on the learned Koopman operator is proposed. The detailed case

studies are conducted in Section V. Section VI concludes this paper and discusses future work.

II. DC Electric Distribution Network Modeling

The DC EDN is better suited to hosting EV supercharging stations than its AC counterparts due to its higher power conversion efficiency and simpler control architecture [35]. As a result of the accelerating buildout of charging stations, the EDNs are expected to experience a shrunken transient stability margin. With an accurate estimation of the ROAs, the distribution system operator (DSO) can maintain a good understanding of the system operation status and take proper control actions, thereby improving grid reliability and security. In this work, we propose a data-driven method for ROA estimation of EDNs hosting future supercharging stations, based on the Koopman operator theory. According to the ROAs estimated in real-time, the charging requests could be managed to ensure the stable EDN operation. Fig. 1 illustrates a DC EDN connected to an external AC grid. The modeled EDN comprises a battery energy storage system (BESS), a solar PV system, and a few high-power EV chargers, which represent key components of future supercharging stations. The external AC grid and the BESS are responsible for DC voltage regulation and power balancing. Different types of pulse-width modulated (PWM) power converters are employed to interface these distributed assets to the common DC bus. The local controls of distributed assets in this work are based on proportional-integral (PI) control. In what follows, the detailed modeling of each distributed asset is provided.

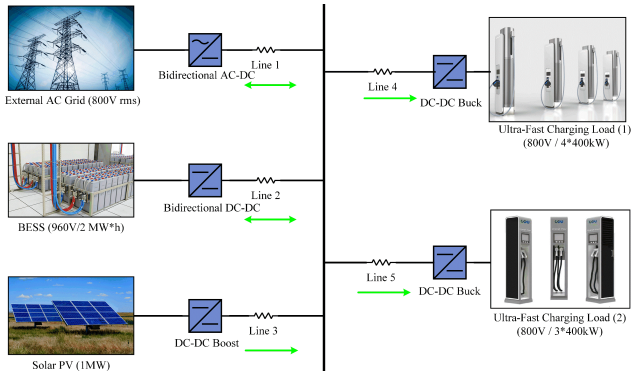

Fig. 1. The modeled DC electric distribution network.

A. Solar PV

A solar PV array in the maximum power point tracking (MPPT) mode is interfaced to the common DC bus through a Boost converter, as shown in Fig. 2. The state equations of the Boost converter are obtained as (1)- (4):

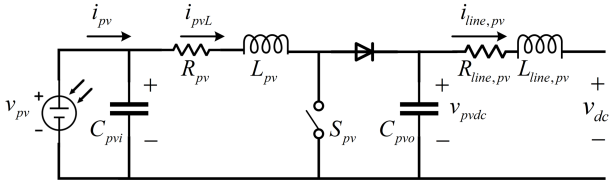

Fig. 2. Solar PV interfaced by a Boost converter.

$$\dot{v}_{pv} = \frac{i_{pv}(v_{pv})}{C_{pvi}} - \frac{i_{pvL}}{C_{pvi}} \tag{1}$$

$$\dot{i}_{pvL} = \frac{-R_{pv}\cdot i_{pvL}}{L_{pv}} + \frac{v_{pv}}{L_{pv}} - \frac{[1-d_{pv}(v_{pv})]\cdot v_{pvdc}}{L_{pv}} \tag{2}$$

$$\dot{v}_{pvdc} = \frac{-i_{line,pv}}{C_{pvo}} + \frac{[1-d_{pv}(v_{pv})]\cdot i_{pvL}}{C_{pvo}} \tag{3}$$

$$\dot{i}_{line,pv} = \frac{-R_{line,pv}\cdot i_{line,pv}}{L_{line,pv}} + \frac{v_{pvdc}}{L_{line,pv}} - \frac{v_{dc}}{L_{line,pv}} \tag{4}$$

where v_{pv} and i_{pv} represent the equivalent output voltage and current of the solar PV system, respectively. As v_{pv} and i_{pv} satisfy a transcendental equation [36], i_{pv} is considered as an implicit function of v_{pv}, denoted as $i_{pv}(v_{pv})$. C_{pvi} is the input capacitor, R_{pv} is the internal resistance of the inductor L_{pv}, and v_{pvdc} is the voltage of the DC-link capacitor C_{pvo}. v_{dc} is the common DC bus voltage. The Perturb and Observe (P&O) technique is employed for MPPT. $d_{pv}(v_{pv})$ denotes the duty cycle to the switch S_{pv} generated by a local PI controller that regulates v_{pv} to the MPPT voltage v_{mpp} [37]. In practice, another BESS could be added in parallel with this solar PV to form a hybrid system such that the uncertainty in solar irradiance could be greatly mitigated. As such, this work assumes small variations in solar irradiance for the modeled PV array.

B. BESS

A bidirectional Buck-Boost converter connects a BESS to the common DC bus of the EDN, as shown in Fig. 3. This BESS can help reduce peak demand charges and provide ancillary services for improved grid stability.

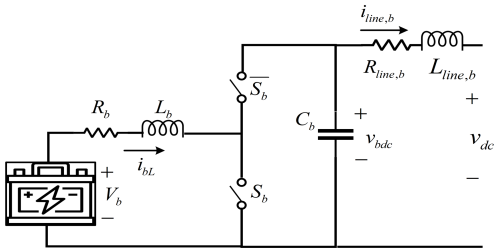

Fig. 3. BESS interfaced by a bidirectional DC-DC converter.

The following equations represent the BESS dynamics:

$$\dot{i}_{bL} = \frac{V_b}{L_b} - \frac{R_b\cdot i_{bL}}{L_b} - \frac{[1-d_b(v_{bdc},i_{bL})]\cdot v_{bdc}}{L_b} \tag{5}$$

$$\dot{v}_{bdc} = \frac{-i_{line,b}}{C_b} + \frac{[1-d_b(v_{bdc},i_{bL})]\cdot i_{bL}}{C_b} \tag{6}$$

$$\dot{i}_{line,b} = \frac{-R_{line,b}\cdot i_{line,b}}{L_{line,b}} + \frac{v_{bdc}}{L_{line,b}} - \frac{v_{dc}}{L_{line,b}} \tag{7}$$

where V_b is the BESS terminal voltage, i_{bL} is the inductor current, v_{bdc} is the voltage of the DC-link capacitor C_b, and $i_{line,b}$ is the output current. $R_{line,b}$ and $L_{line,b}$ are the line resistance and inductance. Since the BESS generally has a large energy capacity and small voltage variations, V_b can be considered as constant. A dual-loop PI control is implemented locally, where the outer loop regulates v_{bdc} to $(V_n - r_b i_{line,b})$ (V_n is the rated common DC bus voltage, and r_b is the DC droop coefficient) and the inner loop regulates i_{bL}. $d_b(v_{bdc}, i_{bL})$

represents the duty cycle generated by the inner current loop. The upper and lower switches of the power converter are then driven in a complementary manner.

C. EV Charging Load

Various charging technologies [38] can be utilized to charge EVs, e.g., constant power (CP) mode, constant current (CC) mode, constant voltage (CV) mode, and their combinations. An EV is charged via a Buck converter, as depicted in Fig. 4.

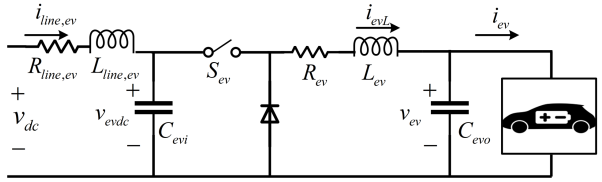

Fig. 4. EV charged via a Buck converter.

The dynamical model is described as

$$\dot{i_{line,ev}} = \frac{-R_{line,ev}\cdot i_{line,ev}}{L_{line,ev}} + \frac{v_{dc}}{L_{line,ev}} - \frac{v_{evdc}}{L_{line,ev}} \tag{8}$$

$$\dot{v}_{evdc} = \frac{i_{line.ev}}{C_{evi}} - \frac{d_{ev}(v_{ev},i_{evL})\cdot i_{evL}}{C_{evi}} \tag{9}$$

$$\dot{i_{evL}} = \frac{-R_{ev}\cdot i_{evL}}{L_{ev}} - \frac{v_{ev}}{L_{ev}} + \frac{d_{ev}(v_{ev},i_{evL})\cdot v_{evdc}}{L_{ev}} \tag{10}$$

$$\dot{v}_{ev} = \frac{i_{evL}}{C_{evo}} - \frac{i_{ev}(v_{ev})}{C_{evo}} \tag{11}$$

where C_{evi} is the input DC-link capacitor, v_{evdc} is its voltage, i_{evL} is the inductor current, i_{ev} is the charging current, and v_{ev} is the EV battery terminal voltage. Depending on the charging mode, the local controller executes single-loop or dual-loop PI control to generate the duty cycle d_{ev} for the switch S_{ev}. As v_{ev} and i_{ev} are solely related to each other in the generic battery model [39], i_{ev} is considered as a function of v_{ev}, i.e., $i_{ev}(v_{ev})$.

D. Grid-Interface Bidirectional AC-DC Converter

The grid-interface converter is implemented using a voltage source converter (VSC) topology. In Fig. 5, v_{ga}, v_{gb} and v_{gc} are the three-phase AC grid voltages, which are assumed to be balanced. L_g is the inductance of the filter on each phase, and R_g is its internal resistance. In addition, v_{gdc} is the voltage of the DC-link capacitor C_g. The external AC grid can absorb or release DC power to assist the DC EDN operation.

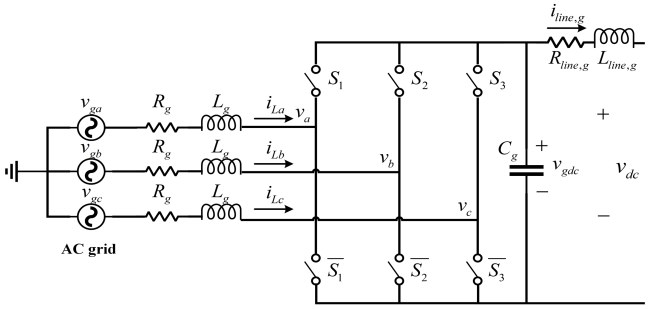

Fig. 5. AC grid interfaced to EDN via an AC-DC converter.

In the synchronously rotating *d-q* reference frame, the state equations related to the inductor filters are given:

$$\dot{i_{Ld}} = \omega \cdot i_{Lq} - \frac{R_g\cdot i_{Ld}}{L_g} + \frac{v_{gd}}{L_g} - \frac{m_d(v_{gdc},i_{Ld})\cdot v_{gdc}}{2L_g} \tag{12}$$

$$\dot{i_{Lq}} = -\omega \cdot i_{Ld} - \frac{R_g\cdot i_{Lq}}{L_g} + \frac{v_{gq}}{L_g} - \frac{m_q(i_{Lq})\cdot v_{gdc}}{2L_g} \tag{13}$$

where v_{gd} and v_{gq} are the grid voltages on the *d-q* axes. i_{Ld} and i_{Lq} are the *d-q* axes currents flowing through the inductor filters, while ω is the measured angular frequency of the AC grid. Besides, a dual-loop PI control [40] is implemented. In the outer voltage control loop, v_{gdc} is regulated to its rated value V_n, which provides the *d*-axis current reference. Since no reactive power is delivered, the *q*-axis current reference is set as zero. The inner current control loop tracks the current references and generates the *d-q* axes duty cycles $m_d(v_{gdc}, i_{Ld})$ and $m_q(i_{Lq})$. The dynamics of the DC link can be expressed based on the power balance between the AC and DC sides. In addition, the line current at the output terminal is obtained.

$$\dot{v}_{gdc} = \frac{3(v_{gd}\cdot i_{Ld}+v_{gq}\cdot i_{Lq})}{2C_g\cdot v_{gdc}} - \frac{i_{line,g}}{C_g} \tag{14}$$

$$\dot{i_{line,g}} = \frac{-R_{line,g}\cdot i_{line,g}}{L_{line,g}} + \frac{v_{gdc}}{L_{line,g}} - \frac{v_{dc}}{L_{line,g}} \tag{15}$$

The dynamics of the AC grid can be represented by the following equations mimicking an equivalent SG [41]:

$$\dot{\omega} = \frac{1}{J}[T_m - \frac{3}{2\omega}(v_{gd}\cdot i_{Ld} + v_{gq}\cdot i_{Lq})] \tag{16}$$

$$\dot{T}_m = -\frac{T_m}{\tau_{pm}} + \frac{P_c}{\tau_{pm}} - \frac{1}{r_D\cdot\tau_{pm}}\cdot(\frac{\omega}{\omega_s} - 1) \tag{17}$$

where ω is the angular frequency, J is the total moment of inertia of the AC grid, and T_m is the mechanical torque provided by the prime mover. Moreover, τ_{pm} is the time constant of the prime mover, while r_D is the speed droop coefficient. ω_s is the rated angular frequency. P_c is the power change setting typically dispatched by the DSO, and in this paper, it is set by a PI controller acting on the error between ω_s and ω. Because the SG stator terminal voltages are also the grid voltages, v_{gd} and v_{gq} in the above equations can be further expressed as

$$v_{gd} = -R_a \cdot i_{Ld} + \omega \cdot L_{aq} \cdot i_{Lq} + v_{sd} \tag{18}$$

$$v_{gq} = -R_a \cdot i_{Lq} - \omega \cdot L_{ad} \cdot i_{Ld} + v_{sq} \tag{19}$$

where R_a, L_{ad}, and L_{aq} are the resistance and *d-q* axes inductances of the SG stator, respectively. v_{sd} and v_{sq} are the voltages induced on the stator by the excitation system. Since voltage regulation can have fast response, v_{gd} and v_{gq} are regarded as constant during transients.

Without loss of generality, it is assumed there are n_{pv} solar PVs, n_b BESSs, n_{ev} EV loads in the DC EDN connected to the external AC grid. The entire DC EDN represents a nonlinear dynamical system:

$$\dot{\boldsymbol{x}} = \boldsymbol{f}_{edn}(\boldsymbol{x}) \tag{20}$$

with state vector $\boldsymbol{x} := [\boldsymbol{x}_{pv}, \boldsymbol{x}_b, \boldsymbol{x}_{ev}, \boldsymbol{x}_{gic}]^T$. Specifically, $\boldsymbol{x}_{pv} := [v_{pv,1}, i_{pvL,1}, \dots, v_{pv,n_{pv}}, i_{pvL,n_{pv}}, v_{pvdc,n_{pv}}, i_{line,pv,n_{pv}}]$,
$\boldsymbol{x}_b := [i_{bL,1}, v_{bdc,1}, i_{line,b,1}, \dots, i_{bL,n_b}, v_{bdc,n_b}, i_{line,b,n_b}]$,
$\boldsymbol{x}_{ev} :=$
$[i_{line,ev,1}, v_{evdc,1}, \dots, i_{line,ev,n_{ev}}, v_{evdc,n_{ev}}, i_{evL,n_{ev}}, v_{ev,n_{ev}}]$,

and $\boldsymbol{x}_{gic} := [i_{Ld}, i_{Lq}, v_{gdc}, i_{line,g}, \omega, T_m]$.

Remark 1: A priori knowledge of the nominal model parameters of (20) is not necessary for a data-driven method. Even if these parameters are available, the actual system is likely to experience deviations from them during operations. Besides, detailed knowledge of the control algorithms is not needed as long as they are related to the system states. However, information on the model structure can reveal the physics of the dynamical system and is thus conducive to data collection for Koopman operator approximation. Furthermore, knowledge of the normal operating ranges of the EDN dynamic states, which can be estimated empirically or from historical system operation data, is helpful in implementing the proposed data-driven ROA estimation approach, as will be presented later.

III. A Stable Koopman Operator

Considering a general dynamical system in the form of

$$\dot{\boldsymbol{x}}(t) = \boldsymbol{f}(\boldsymbol{x}(t)) \tag{21}$$

where $\boldsymbol{x}$ evolves in a state space $\boldsymbol{\mathcal{X}} \subset \boldsymbol{\mathcal{R}}^p$. Let $\boldsymbol{F}(\boldsymbol{x}, t)$ be the flow of the continuous-time system (21) starting from an initial state $\boldsymbol{x}_0$ when $t \geq 0$, and $g : \boldsymbol{\mathcal{X}} \to \boldsymbol{\mathcal{C}}$ be a measurable function referred to as the observable or a basis function. All observables constitute the space of observables $\boldsymbol{\mathcal{F}}$. The Koopman operator $\boldsymbol{K}^t : \boldsymbol{\mathcal{F}} \to \boldsymbol{\mathcal{F}}$ for (21) advances an observable based on the evolution of the trajectories in $\boldsymbol{\mathcal{X}}$ such that

$$(\boldsymbol{K}^t g\,)(\boldsymbol{x}) = g \circ \boldsymbol{F}(\boldsymbol{x}, t) \tag{22}$$

where $\circ$ represents the pointwise function composition. Since the Koopman operator is linear over its observables, it can be characterized by eigen-decomposition. In general, an eigenfunction φ and its eigenvalue $\lambda \in \boldsymbol{\mathcal{C}}$ satisfy:

$$(\boldsymbol{K}^t \varphi)(\boldsymbol{x}) = \varphi \circ \boldsymbol{F}(\boldsymbol{x}, t) = exp(\lambda t)\varphi(\boldsymbol{x}) \tag{23}$$

In addition, the Koopman operator embeds the finite-dimensional nonlinear dynamics (21) to an infinite-dimensional function space, so it is more practical to approximate this infinite-dimensional operator using data-driven methods such as dynamic mode decomposition (DMD), EDMD, generalized Laplace averages, deep neural networks (DNNs), etc. Among them, EDMD is most widely applied because it uses an extended basis to capture nonlinearities and only needs one-step iteration. More details on the Koopman operator theory and its data-driven methods can be found in [42].

Let $\boldsymbol{\mathcal{F}}_N \subset \boldsymbol{\mathcal{F}}$ be an N-dimensional Koopman invariant subspace, i.e., $\boldsymbol{K}^t\, g \in \boldsymbol{\mathcal{F}}_N$ for any $g \in \boldsymbol{\mathcal{F}}_N$. When EDMD is applied to (21), the basis functions are functions of the states, denoted as $\psi_i(\boldsymbol{x}) \in \boldsymbol{\mathcal{F}}_N$, $i = 1, 2, \dots, N$. Assuming that the DC EDN (20) provides $(M+1)$ consecutive snapshots of the system states from a variety of collected trajectories over uniform time intervals Δt, EDMD constructs a finite-dimensional approximation $\widetilde{\boldsymbol{K}}$ of the Koopman operator by solving the following least-squares problem:

$$\min_{\widetilde{\boldsymbol{K}} \in \boldsymbol{R}^{N \times N}} \|\boldsymbol{\psi}(\boldsymbol{Y}) - \widetilde{\boldsymbol{K}} \cdot \boldsymbol{\psi}(\boldsymbol{X})\|_F^2 = \min_{\widetilde{\boldsymbol{K}} \in \boldsymbol{R}^{N \times N}} \sum_{k=1}^{M} \|\boldsymbol{\psi}(\boldsymbol{x}_{k+1}) - \widetilde{\boldsymbol{K}} \cdot \boldsymbol{\psi}(\boldsymbol{x}_k)\|^2 \tag{24}$$

where $\|\cdot\|_F$ refers to the Frobenius norm of a matrix and $\|\cdot\|$ is the 2-norm of a vector. $\boldsymbol{\psi}(\boldsymbol{Y}) := [\boldsymbol{\psi}(\boldsymbol{x}_2), \dots, \boldsymbol{\psi}(\boldsymbol{x}_{M+1})]$, $\boldsymbol{\psi}(\boldsymbol{X}) := [\boldsymbol{\psi}(\boldsymbol{x}_1), \dots, \boldsymbol{\psi}(\boldsymbol{x}_M)]$, and $\boldsymbol{\psi}(\boldsymbol{x}_k) := [\psi_1(\boldsymbol{x}_k), \dots, \psi_N(\boldsymbol{x}_k)]^T$ at time instant k.

A closed-form solution can be readily obtained as

$$\widetilde{\boldsymbol{K}} = \boldsymbol{A} \cdot \boldsymbol{U}^{\dagger} \tag{25}$$

where † denotes the Moore–Penrose pseudoinverse, $\boldsymbol{A} := \boldsymbol{\psi}(\boldsymbol{Y}) \cdot \boldsymbol{\psi}(\boldsymbol{X})^T$ and $\boldsymbol{U} := \boldsymbol{\psi}(\boldsymbol{X}) \cdot \boldsymbol{\psi}(\boldsymbol{X})^T$. The basis functions can be customized and have multiple choices. To fairly compare with the SOSP, which exhibits less conservativeness than other model-based approaches in ROA estimation, this study uses monomials as the basis functions. Once $\widetilde{\boldsymbol{K}}$ is obtained, the Koopman eigenfunction φ_i corresponding to an eigenpair $(\mu_i, \boldsymbol{v}_i)$ of the transpose of $\widetilde{\boldsymbol{K}}$ is obtained:

$$\varphi_i(\boldsymbol{x}) = \boldsymbol{v}_i^T \cdot \boldsymbol{\psi}(\boldsymbol{x}) \tag{26}$$

Besides, the eigenvalue of $\boldsymbol{K}^t$ corresponding to φ_i is $\lambda_i = \frac{log \mu_i}{\Delta t}$.

However, since $\widetilde{\boldsymbol{K}}$ is used to numerically approximate $\boldsymbol{K}^t$, there will obviously be errors accumulated over a given time span. The actual value of the basis function at certain time step k can be expressed as its approximated value plus the error $\mathcal{E}_k$:

$$\boldsymbol{\psi}(\boldsymbol{x}_k) = \widetilde{\boldsymbol{K}} \cdot \boldsymbol{\psi}(\boldsymbol{x}_{k-1}) + \mathcal{E}_k \tag{27}$$

Likewise,

$$\boldsymbol{\psi}(\boldsymbol{x}_{k-1}) = \widetilde{\boldsymbol{K}} \cdot \boldsymbol{\psi}(\boldsymbol{x}_{k-2}) + \mathcal{E}_{k-1} \tag{28}$$

Iteratively, we obtain a generalized expression at time step k:

$$\boldsymbol{\psi}(\boldsymbol{x}_k) = \widetilde{\boldsymbol{K}}^k \cdot \boldsymbol{\psi}(\boldsymbol{x}_0) + \sum_{i=0}^{k-1} \widetilde{\boldsymbol{K}}^i \cdot \mathcal{E}_{k-i} \tag{29}$$

It follows that the accumulated error $\sum_{i=0}^{k-1} \widetilde{\boldsymbol{K}}^i \cdot \mathcal{E}_{k-i}$ can be bounded based on the norm properties:

$$\left\|\sum_{i=0}^{k-1} \widetilde{\boldsymbol{K}}^i \cdot \mathcal{E}_{k-i}\right\| \leq \sum_{i=0}^{k-1} \left\|\widetilde{\boldsymbol{K}}^i \cdot \mathcal{E}_{k-i}\right\| \leq \sum_{i=0}^{k-1} \left\|\widetilde{\boldsymbol{K}}^i\right\| \cdot \|\mathcal{E}_{k-i}\| \leq \sum_{i=0}^{k-1} \left\|\widetilde{\boldsymbol{K}}\right\|^i \cdot \|\mathcal{E}_{k-i}\| \tag{30}$$

If $\|\mathcal{E}_i\| \leq e_{max}$ for any i, then

$$\left\|\sum_{i=0}^{k-1} \widetilde{\boldsymbol{K}}^i \cdot \mathcal{E}_{k-i}\right\| \leq e_{max} \cdot \sum_{i=0}^{k-1} \left\|\widetilde{\boldsymbol{K}}\right\|^i \tag{31}$$

Inequality (31) shows that the accumulated approximation error could be enlarged exponentially if the learned Koopman operator $\widetilde{\boldsymbol{K}}$ is unstable. Inspired by [33] and [34], we propose to apply the SOC algorithm to learn a stable Koopman operator in light of its superior numerical stability over long time horizons, memory efficiency, and scalability. Specifically, the matrix $\widetilde{\boldsymbol{K}}$ is stable if and only if it can be expressed as $\widetilde{\boldsymbol{K}} = \boldsymbol{S}^{-1} \cdot \boldsymbol{O} \cdot \boldsymbol{C} \cdot \boldsymbol{S}$, where $\boldsymbol{S}$ is positive definite, $\boldsymbol{O}$ is orthogonal, and $\boldsymbol{C}$ is positive semidefinite contraction (i.e., the singular values of $\boldsymbol{C}$ are less than or equal to 1). Hence, instead of solving (24) in EDMD, the following optimization problem is solved using the fast projected gradient descent method presented in [33]:

$$\inf_{\widetilde{\boldsymbol{K}}} \|\boldsymbol{\psi}(\boldsymbol{Y}) - \widetilde{\boldsymbol{K}} \cdot \boldsymbol{\psi}(\boldsymbol{X})\|_F^2 = \inf_{\boldsymbol{S},\boldsymbol{O},\boldsymbol{C}} \|\boldsymbol{\psi}(\boldsymbol{Y}) - \boldsymbol{S}^{-1} \cdot \boldsymbol{O} \cdot \boldsymbol{C} \cdot \boldsymbol{S} \cdot \boldsymbol{\psi}(\boldsymbol{X})\|_F^2 \tag{32}$$

The gradients with respect to the matrices $\boldsymbol{S}$, $\boldsymbol{O}$, and $\boldsymbol{C}$ are derived as:

$$\nabla_S f(\boldsymbol{S},\boldsymbol{O},\boldsymbol{C}) = \boldsymbol{S}^{-T}(\boldsymbol{W}\cdot\boldsymbol{E}^T - \boldsymbol{E}^T\cdot\boldsymbol{W}) \quad (33)$$

$$\nabla_O f(\boldsymbol{S},\boldsymbol{O},\boldsymbol{C}) = -\boldsymbol{S}^{-T}\cdot\boldsymbol{W}\cdot\boldsymbol{S}^T\cdot\boldsymbol{C}^T \quad (34)$$

$$\nabla_C f(\boldsymbol{S},\boldsymbol{O},\boldsymbol{C}) = -\boldsymbol{O}^T\cdot\boldsymbol{S}^{-T}\cdot\boldsymbol{W}\cdot\boldsymbol{S}^T \quad (35)$$

where $\boldsymbol{E} := \boldsymbol{S}^{-1}\cdot\boldsymbol{O}\cdot\boldsymbol{C}\cdot\boldsymbol{S}$ and $\boldsymbol{W} := [\boldsymbol{\psi}(\boldsymbol{Y}) - \boldsymbol{E}\cdot\boldsymbol{\psi}(\boldsymbol{X})]\cdot\boldsymbol{\psi}(\boldsymbol{X})^T$. This algorithm enforces stability by projecting the solution onto the feasible set and iteratively updates the gradient directions. Thus, the stability constraint is naturally imposed on $\widetilde{\boldsymbol{K}}$. And (26) can still be utilized to derive the Koopman eigenfunctions.

Remark 2: Under the Koopman operator framework, the Koopman eigenfunctions can be leveraged to construct Lyapunov candidate functions in a systematic way with strict stability guarantees. In the following, the derived Koopman eigenfunctions will be used to constitute a linear space of Lyapunov candidate functions, and the union of sublevel sets of the decided Lyapunov functions will provide an inner approximation to the actual ROA.

IV. Data-Driven ROA Estimation

When an equilibrium state $\boldsymbol{x}^*$ of the dynamical system (21) is nonzero, any system state $\boldsymbol{x}$ can be translated to $\boldsymbol{x}$ - $\boldsymbol{x}^*$. Therefore, $\boldsymbol{x}^*$ is assumed as the origin for simplicity. If the origin is asymptotically stable but not globally attractive, it is desirable to know which trajectories will converge to it as time approaches infinity. The ROA of the system equilibrium state $\boldsymbol{x}^* = \boldsymbol{0}$ for (21) is mathematically defined as a set $ROA_{\boldsymbol{x}^*=\boldsymbol{0}} := \left\{\boldsymbol{x}\in\mathcal{R}^p : \lim_{t\to\infty}\boldsymbol{F}(\boldsymbol{x},t) = \boldsymbol{0}\right\}$. Furthermore, the γ-sublevel set $\boldsymbol{\Omega}_{V,\gamma}$ of a Lyapunov function $V(\boldsymbol{x})$ with a positive γ is defined as $\boldsymbol{\Omega}_{V,\gamma} = \{\boldsymbol{x}\in\mathcal{R}^p : V(\boldsymbol{x}) \le \gamma\}$, which can practically characterize the forward invariant subsets of the actual ROA [7]. If the following conditions are satisfied:

1) $\boldsymbol{\Omega}_{V,\gamma}$ is bounded
2) $V(\boldsymbol{0}) = 0$ and $V(\boldsymbol{x}) > 0$ for all $\boldsymbol{x}\in\mathcal{R}^p$
3) $\boldsymbol{\Omega}_{V,\gamma}\setminus\{\boldsymbol{0}\} \subset \left\{\boldsymbol{x}\in\mathcal{R}^p : \dot{V}(\boldsymbol{x}) = \frac{\partial V(\boldsymbol{x})}{\partial \boldsymbol{x}}\cdot\boldsymbol{f}(\boldsymbol{x}) < 0\right\}$

(36)

then the flow $\boldsymbol{F}(\boldsymbol{x},t)$ of (21) exists and $\boldsymbol{F}(\boldsymbol{x},t)\in\boldsymbol{\Omega}_{V,\gamma}$ holds for all $\boldsymbol{x}\in\boldsymbol{\Omega}_{V,\gamma}$ and $t\ge 0$. In addition, $\lim_{t\to\infty}\boldsymbol{F}(\boldsymbol{x},t) = \boldsymbol{0}$. Accordingly, $\boldsymbol{\Omega}_{V,\gamma}$ is an invariant subset of $ROA_{\boldsymbol{x}^*=\boldsymbol{0}}$.

The details of the proposed data-driven ROA estimation are elaborated in Fig. 6 below. Both historical system operation data recorded by measurement devices such as phasor measurement units (PMUs) and simulation data generated from high-fidelity numerical simulations can serve as the required measured data for this method. Firstly, the measured data are employed by the SOC algorithm to approximate the Koopman eigenfunctions as explained in Section III; secondly, the Lyapunov candidate functions are linearly parameterized using the learned Koopman eigenfunctions; thirdly, polytope constraints are formed; and finally, a tight inner estimation to the actual ROA is obtained.

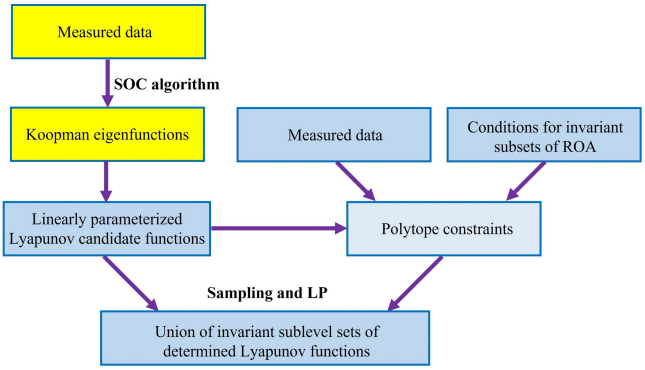

Fig. 6. Flowchart of proposed data-driven ROA estimation.

Under the assumption that large amounts of measured data are available, our goal is to estimate the ROA of the DC EDN (20) in a data-driven fashion. Fig. 7 illustrates how to apply the conditions in (36) to various trajectory data to find a Lyapunov function and its γ-sublevel set.

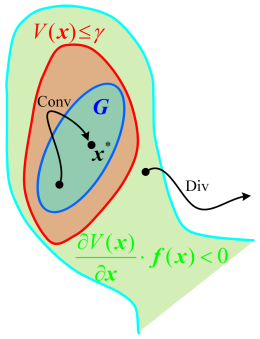

Fig. 7. Illustration diagram of ROA inner estimation.

Suppose there exists a Lyapunov function $V(\boldsymbol{x})$ to certify that a set $\boldsymbol{G}$ lies inside the ROA. As is observed from Fig. 7, $V(\boldsymbol{x}) \le \gamma$ and $\dot{V}(\boldsymbol{x}) < 0$ should hold for a convergent trajectory starting from $\boldsymbol{G}$, while $V(\boldsymbol{x}) > \gamma$ is satisfied for a divergent trajectory starting from $\boldsymbol{G}$'s complement $\boldsymbol{G}^c$. Also, $\boldsymbol{G}$ will not be within the ROA if at least one trajectory eventually diverges with initial conditions in $\boldsymbol{G}$. Thus, a smaller region of $\boldsymbol{G}$ should be chosen.

Conventionally, it is computationally intensive if not intractable for those optimization-based methods such as the SOSP to calculate the maximum ROA, when dealing with many decision variables due to the high dimension of an EDN, not to mention the lifted space $\mathcal{F}_N$. To address this issue, we propose to reduce the number of decision variables for ROA estimation via linearly parameterizing an arbitrary Lyapunov candidate function using the Koopman eigenfunctions from Section III. Specifically, we select a set of Koopman eigenfunctions φ_i $(i = 1, 2, \dots, N_\phi)$ with a sufficiently large negative real part $\mathrm{Re}[\lambda_i]$ to construct the basis $\phi_i(\boldsymbol{x})$ of the linear space for Lyapunov candidate functions, as such eigenfunctions can capture the stability properties of the underlying dynamical system [27]. Further, if the basis function is chosen as $\phi_i(\boldsymbol{x}) := \varphi_i(\boldsymbol{x})\cdot\bar{\varphi}_i(\boldsymbol{x}) = |\varphi_i(\boldsymbol{x})|^2$ (the overbar denotes complex conjugation), then $\phi_i(\boldsymbol{x}) \ge 0$ and $\dot{\phi}_i(\boldsymbol{x}) = 2\cdot\mathrm{Re}[\lambda_i]\cdot|\varphi_i(\boldsymbol{x})|^2 = 2\cdot\mathrm{Re}[\lambda_i]\cdot\phi_i(\boldsymbol{x}) \le 0$ hold for $i = 1, 2, \dots, N_\phi$. It follows from the detailed proof in the Appendix that the family

of sets $\boldsymbol{\mathcal{V}}_\gamma = \left\{\boldsymbol{x} \in \boldsymbol{\mathcal{R}}^p : \sum_{i=1}^{N_\phi} \alpha_i \cdot \phi_i(\boldsymbol{x}) \le \gamma\right\}$ with $\alpha_i > 0$ are forward invariant.

Consider a Lyapunov candidate function $V(\boldsymbol{x}) = \sum_{i=1}^{N_\phi} \alpha_i \cdot \phi_i(\boldsymbol{x})$, where the coefficients α_i are to be determined. When the conditions discussed in (36) and observed in Fig. 7 are strictly imposed on the trajectory data, they could be naturally translated into constraints on α_i in a LP problem. It should also be noted that the above constructed Lyapunov candidate function will lead to stronger expressive power and thus a less conservative ROA approximation when higher-degree monomials are adopted for $\psi_i(\boldsymbol{x})$, compared to the conventional quadratic Lyapunov functions used in the T-S multi-modeling.

To seek a Lyapunov function whose γ-sublevel set is forward invariant, numerous trajectory data need to be sampled initially from a prechosen set $\boldsymbol{G}$. In practice, $\boldsymbol{G}$ for an EDN is related to the allowable operating ranges of each dynamic state variable. For instance, the typical frequency of islanded microgrids lies between 59.3 and 60.5 Hz, while the DC common bus voltage is $\pm 5\%$ of the rated value. However, $\boldsymbol{G}$ should be shrunk accordingly once divergent trajectories beginning from $\boldsymbol{G}$ are detected. Based on the condition $\boldsymbol{\mathcal{V}}_\gamma \setminus \{\boldsymbol{0}\} \subset \left\{\boldsymbol{x} \in \boldsymbol{\mathcal{R}}^p : \dot{V}(\boldsymbol{x}) < 0\right\}$, there should be $\dot{V}(\boldsymbol{x}) \le \beta \cdot [\gamma - V(\boldsymbol{x})]$ for the convergent trajectory data with initial conditions in $\boldsymbol{G}$, where β is a positive constant and can be initially set as twice the minimum of $|\mathrm{Re}[\lambda_i]|$. Thus, on a convergent trajectory $[\boldsymbol{x}_0, \boldsymbol{x}_1, \dots, \boldsymbol{x}_T]$ with $(T+1)$ time steps, any data point $\boldsymbol{x}_k$ should satisfy 1) $\sum_{i=1}^{N_\phi} \alpha_i \cdot \phi_i(\boldsymbol{x}_k) \le \gamma$; 2) $\sum_{i=1}^{N_\phi} \alpha_i \cdot \dot{\phi}_i(\boldsymbol{x}_k) + \beta \cdot \left[\sum_{i=1}^{N_\phi} \alpha_i \cdot \phi_i(\boldsymbol{x}_k) - \gamma\right] \le 0$. In compact matrix form, the constraints are

$$\boldsymbol{\Phi} \cdot \boldsymbol{\alpha} \le \boldsymbol{0} \tag{37.1}$$

$$(\boldsymbol{\Phi}_{dot} + \beta \cdot \boldsymbol{\Phi}) \cdot \boldsymbol{\alpha} \le \boldsymbol{0} \tag{37.2}$$

$$\boldsymbol{\alpha} \ge \boldsymbol{\delta} \tag{37.3}$$

$$\boldsymbol{\alpha}[1{:}N_\phi] \le \boldsymbol{1} \tag{37.4}$$

$$[1 \quad 1 \dots \quad 1 \quad 0] \cdot \boldsymbol{\alpha} \ge 1 \tag{37.5}$$

where $\boldsymbol{\Phi} \coloneqq \begin{bmatrix} \phi_1(\boldsymbol{x}_0) & \phi_2(\boldsymbol{x}_0) & \cdots & \phi_{N_\phi}(\boldsymbol{x}_0) & -1 \\ \vdots & & \ddots & \vdots & \\ \phi_1(\boldsymbol{x}_T) & \phi_2(\boldsymbol{x}_T) & \cdots & \phi_{N_\phi}(\boldsymbol{x}_T) & -1 \end{bmatrix}$, $\boldsymbol{\Phi}_{dot} \coloneqq \begin{bmatrix} \dot{\phi}_1(\boldsymbol{x}_0) & \dot{\phi}_2(\boldsymbol{x}_0) & \cdots & \dot{\phi}_{N_\phi}(\boldsymbol{x}_0) & 0 \\ \vdots & & \ddots & \vdots & \\ \dot{\phi}_1(\boldsymbol{x}_T) & \dot{\phi}_2(\boldsymbol{x}_T) & \cdots & \dot{\phi}_{N_\phi}(\boldsymbol{x}_T) & 0 \end{bmatrix}$, and $\boldsymbol{\alpha} \coloneqq \left[\alpha_1 \ \alpha_2 \dots \alpha_{N_\phi} \ \gamma\right]^T$. $\boldsymbol{\delta}$ is a vector with all fixed small positive constants δ for tightness.

However, a divergent trajectory starting from the complement of $\boldsymbol{G}$ should obey

$$\boldsymbol{\Phi} \cdot \boldsymbol{\alpha} \ge \boldsymbol{\delta} \tag{37.6}$$

Each row of the above constraints defines a half-space in $\boldsymbol{\mathcal{R}}^{N_\phi+1}$ and the intersection of these half-spaces defines a feasible polytope [43]. As more trajectories are considered, the feasible polytope will be iteratively refined with a monotonic decrease in volumes. Theoretically, it will converge to a certain convex polytope $\boldsymbol{\mathcal{P}}$ as the number of iterations approaches infinity. The detailed ROA estimation algorithm is presented as:

PROPOSED ROA ESTIMATION ALGORITHM

Stage 1: Create a feasible polytope $\boldsymbol{\mathcal{P}}$ using measured data	
Initialize: $\boldsymbol{G}$, $\boldsymbol{A}_c$, $\boldsymbol{A}_d$, ρ, β, and δ	
Obtain K_{max} data trajectories:	
1	$k = 0$, $K_c = 0$, and $K_d = 0$
2	while $k < K_{max}$:
3	sample a random initial state $\boldsymbol{x}_{0k}$ from $\boldsymbol{G}$
4	if a trajectory from $\boldsymbol{x}_{0k}$ converges:
5	save this trajectory in $\boldsymbol{A}_c$, and $K_c \mathrel{+}= 1$
6	else:
7	save this trajectory in $\boldsymbol{A}_d$, and $K_d \mathrel{+}= 1$
8	$k \mathrel{+}= 1$
Apply constraints (37.1~37.6) to the data trajectories:	
9	$\boldsymbol{\mathcal{P}} = \{\boldsymbol{\alpha} \in \boldsymbol{\mathcal{R}}^{N_\phi+1} : (37.3) - (37.5)\}$
10	for $i = 1{:}K_c$:
11	form polytope $\boldsymbol{\mathcal{P}}_i$ based on (37.1), (37.2) using $\boldsymbol{A}_c(i)$
12	$\boldsymbol{\mathcal{P}}_i \leftarrow \boldsymbol{\mathcal{P}} \cap \boldsymbol{\mathcal{P}}_i$
13	if *is_empty*($\boldsymbol{\mathcal{P}}_i$):
14	$\beta \leftarrow \rho \cdot \beta$
15	go to Line 10
16	$\boldsymbol{\mathcal{P}} \leftarrow \boldsymbol{\mathcal{P}}_i$
17	for $i = 1{:}K_d$:
18	use $\boldsymbol{x}_{0i}$ of $\boldsymbol{A}_d(i)$ as a new vertex and project as $\boldsymbol{G}_i$
19	$\boldsymbol{G} \leftarrow \boldsymbol{G}_i$
20	form polytope $\boldsymbol{\mathcal{P}}_i$ based on (37.6) using $\boldsymbol{A}_d(i)$
21	$\boldsymbol{\mathcal{P}} \leftarrow \boldsymbol{\mathcal{P}} \cap \boldsymbol{\mathcal{P}}_i$
Stage 2: Determine $\boldsymbol{\mathcal{V}}_\gamma$ via sampling and linear optimization	
Initialize: $\boldsymbol{\mathcal{V}}_\gamma = \emptyset$	
22	$j = 0$
23	while $j < N_{max}$:
24	sample $\boldsymbol{x}_j$ from $\boldsymbol{G}$
25	solve: $\max_{\boldsymbol{\alpha}} \sum_{i=1}^{N_\phi} \alpha_i \cdot \phi_i(\boldsymbol{x}_j) - \gamma$
26	$s.t.\ \ \boldsymbol{\alpha} \subseteq \boldsymbol{\mathcal{P}}$
27	$\boldsymbol{\mathcal{V}}_{\gamma,j} = \left\{\boldsymbol{x} \in \boldsymbol{\mathcal{R}}^p : \sum_{i=1}^{N_\phi} \alpha_i \cdot \phi_i(\boldsymbol{x}) \le \max\{\gamma + obj_{max}, \gamma\}\right\}$
28	$\boldsymbol{\mathcal{V}}_\gamma \leftarrow \boldsymbol{\mathcal{V}}_\gamma \cup \boldsymbol{\mathcal{V}}_{\gamma,j}$
29	$j \ = j + 1$

The proposed ROA estimation algorithm consists of two stages, given the already learned Koopman eigenfunctions from Section III. In Stage 1, measured data are utilized to construct a feasible polytope. If historical system operation data are not readily available, trajectory data can also be generated through high-fidelity numerical simulations. If runtime is of concern, a time limit can be set rather than K_{max}. Then the actual number of simulated trajectory data will be applied. During this process, the K_c convergent trajectories and K_d divergent trajectories will be stored in arrays $\boldsymbol{A}_c$ and $\boldsymbol{A}_d$, respectively. In Line 14, the preset β is amplified by a constant parameter ρ once the

intersection of intermediate polytopes becomes empty. As is shown in Line 18, the disqualified initial state is used as a new vertex, whose projections on the coordinate axis of each state attain $\boldsymbol{G}_i$. A tight polytope $\boldsymbol{\mathcal{P}}$ could be finally obtained in Line 21. In Stage 2, a set of $\boldsymbol{x}$'s are sampled from the refined $\boldsymbol{G}$ and LP problems are solved on each $\boldsymbol{x}$ to derive the invariant sub-level sets $\boldsymbol{\mathcal{V}}_\gamma$ (in Line 27) of each Lyapunov candidate function; obj_{max} represents the maximum of the objective function in Line 25. Theoretically, for a sufficiently large number of samples N_{max}, $\boldsymbol{\mathcal{V}}_\gamma$ will converge and cover the largest sub-level set of a single Lyapunov function that is based on the SOSP [17]. Furthermore, the proposed ROA estimation can be even closer to the actual one if obj_{max} is positive. It is also noteworthy that different sampling techniques can lead to different convergence rates. The efficient high-dimensional sampling method named the Dikin Walk [44] can be adopted to generate uniform random samples for Lines 3 and 24. Lastly, both stages in the proposed algorithm are highly parallelizable and parallel computing can be leveraged for speedup in simulation and optimization.

V. Case Studies

To verify the effectiveness of the proposed data-driven approach for ROA estimation, numerical simulations of a 2-kV DC EDN as shown in Fig. 1 are conducted in MATLAB/Simulink with a fixed step size of 50 μs. MATLAB Parallel Computing Toolbox and Parallel Server are leveraged to expedite simulations. The SG representing the external AC grid is rated at 5 MVA, and two (n_{ev}) aggregated EV charging loads are considered. Averaged modeling [45] for the PWM power converters is implemented. The detailed system parameters are given in Table I. The EV battery models in the simulations have low initial state of charge (SoC) values and are only charged in the CP mode for simplicity. Also, an EV's arrival and departure times are assumed to follow the truncated normal distributions suggested by [46]. In Fig. 1, each simulated EV charging load represents one charger with a variable number of charging ports. For instance, the Ultra-Fast Charging Load (2) represents three charging ports, with possible charging power levels of 0 kW (idle), 400 kW (for 1 EV), 800 kW (for 2 EVs), or 1200 kW (for 3 EVs). The duration of each level of charging power can be determined by the overlapping of EVs' arrival and departure times. In the preset $\boldsymbol{G}$, ω is $0.995\omega_s$~$1.005\omega_s$, T_m is from 0 to 1.1 times the rated value, the DC-link voltages are $0.95V_n$~$1.05V_n$, the unidirectional inductor currents are from 0 to 1.2 times the rated values, and the range of bidirectional inductor currents is ±1.2 times the rated values. Besides, an EV battery terminal voltage corresponds to the SoC range of 10%~60%. Communication latency is ignored during the simulations because the EDNs under consideration usually do not span a large geographic area. In addition, Python interacts with Simulink for data collection and computations. The experiment platform is a high-performance server with an AMD EPYC 7B13 CPU (64 cores) and 512-GB RAM.

Firstly, system operation data are simulated to learn the Koopman eigenfunctions via the SOC algorithm executed in Python. 100 different trajectories are collected with random initial states selected within $\boldsymbol{G}$. Each trajectory lasts for 20 sec and is sampled with $\Delta t = 0.01$ sec. The probability distribution parameters used during each trajectory collection are presented in Table II. Although not a problem in this work, if historical system operation data acquired from field measurement devices are utilized, data corruption could be a concern. Thus, data preprocessing [47] such as data cleaning and statistical processing could be applied to reduce the negative effects of noise and outliers in the raw data. Additional techniques including regularization and data augmentation [48] could also be implemented to minimize the potential for data corruption. In this proposed method, the SOC algorithm could be practically executed offline on a regular basis using the most recent state measurements to maintain the high precision of the learned Koopman eigenfunctions.

TABLE I
System Parameters of the DC EDN

Solar PV		**BESS**	
Parameter	Value	Parameter	Value
v_{mpp} at STC	903 V	V_b (rated)	960 V
i_{mpp} at STC	1105.68 A	R_b	0.4 mΩ
R_{pv}	0.3 mΩ	L_b	0.8 mH
L_{pv}	0.5 mH	C_b	3000 μF
C_{pvi}	600 μF	V_n	2000 V
C_{pvo}	2000 μF	r_b	0.085 V/A

STC: standard test conditions

Ultra-Fast Charging Load (1)		**Ultra-Fast Charging Load (2)**	
Parameter	Value	Parameter	Value
v_{ev} (rated)	800 V	v_{ev} (rated)	800 V
R_{ev}	0.25 mΩ	R_{ev}	0.25 mΩ
L_{ev}	0.6 mH	L_{ev}	0.5 mH
C_{evi}	1500 μF	C_{evi}	1500 μF
C_{evo}	1000 μF	C_{evo}	800 μF
Grid-Interfaced VSC		**AC Grid Inductor Filter**	
Parameter	Value	Parameter	Value
C_g	5000 μF	R_g	1 mΩ
		L_g	0.5 mH
Synchronous Generator			
Parameter	Value	Parameter	Value
J (kg· m^2)	3.7×10^6	τ_{pm}	0.2 sec
r_D	0.05 pu		

	Parameter	Value	Parameter	Value
Line 1	$R_{line,g}$	112 mΩ	$L_{line,g}$	0.45 mH
Line 2	$R_{line,b}$	140 mΩ	$L_{line,b}$	0.57 mH
Line 3	$R_{line,pv}$	71.8 mΩ	$L_{line,pv}$	0.31 mH
Line 4	$R_{line,ev,1}$	57.4 mΩ	$L_{line,ev,1}$	0.24 mH
Line 5	$R_{line,ev,2}$	86.2 mΩ	$L_{line,ev,2}$	0.36 mH

TABLE II
STATISTICAL DISTRIBUTION OF EV CHARGING BEHAVIOR

	Distribution	Boundaries
Arrival time (sec)	$\mathcal{N}(3, 1^2)$	$[0, 6]$
Departure time (sec)	$\mathcal{N}(15, 1^2)$	$[13, 18]$

There is always a trade-off between computational cost and expressivity in designing the Lyapunov candidate function when selecting the monomial basis for the SOC algorithm. This study chooses the monomials in $\boldsymbol{x}$ of degree up to 4. As the number of states of the simulated DC EDN is 21, there are 12649 (N) monomial functions in the basis when the special monomial "1" is removed. It takes on average 791.18 sec for the SOC algorithm to obtain the Koopman eigenfunctions based on the concatenated trajectory data. 5368 (N_ϕ) out of 12649 Koopman eigenfunctions are retained after taking $|\mathrm{Re}[\lambda_i]| > \frac{1}{3} \cdot \max|\mathrm{Re}[\lambda_i]|$ to ensure large enough negative real parts. β is determined as 0.0561, ρ is set as 1.07, and δ is $2 \cdot 10^{-16}$.

An extreme scenario is considered, where all EV chargers are in use. At some point, the only two idled EV charging ports at the Ultra-Fast Charging Load (1) request connection to the DC EDN, equivalent to increasing the power level from 800 kW to 1600 kW. To ensure transient stability, the DSO wishes to manage this request by estimating the ROA. Suppose the equilibrium points before and after enabling these charging ports are x_0 = [889.8V, 556.2A, 1959.1V, 252.0A 667.5A, 1965.5V, 344.6A, 411.5A, 1947.3V, 925.2A, 864.7V, 617.4A, 1948.1V, 1373.7A, 873.6V, 884.6A, -0.31A, 2000.0V, 432.3A, 377.0rad/s, 2620.2N·m]^T and x_{eq} =[891.5V, 555.6A, 1932.6V, 255.8A, 1038.7, 1946.4V, 536.3A, 837.7A, 1915.9V, 1834.2A, 872.3V, 626.1A, 1921.4V, 1371.0A, 875.2V, 1378.0A, -2.25A, 1998.8V, 671.8A, 376.8rad/s, 3904.3N·m]^T, respectively. In practice, however, an absolutely stable equilibrium may never exist due to the uncertainties and external disturbances, which makes the quasi-equilibrium determined by model-based methods less accurate. To this end, the in-line sliding-window scheme proposed in [49] could be applied to predict the quasi-equilibrium after assuming a specific EV charger is connected to the DC EDN. However, when the existing measured datasets are insufficient to span a complete data trajectory, the MPC linear predictor in [26] could further be used to extrapolate the evolving state trajectory. Development of such a predictive approach with enhanced prediction accuracy is left for our future research.

Once the Koopman eigenfunctions are learned, the data trajectories under the specific operating condition need to be obtained in Stage 1 of the proposed ROA estimation algorithm. For the EDN Simulink model, a run time of 10 sec is sufficient to determine the convergence of each simulated trajectory. 20 of 10-sec simulation runs are then conducted, and 127 sec are taken to collect the trajectory data. No divergent trajectories commencing from the preset $\boldsymbol{G}$ are found. Nonetheless, the initial β is updated twice to generate a non-empty polytope. In Stage 2, the scipy.optimize and multiprocessing packages of Python are utilized to solve the LP problems in parallel. In addition, the fast and efficient HiGHS solver is chosen. Ideally, if more samples are collected to solve the LP problems, the union of the obtained invariant sets will be even closer to the actual ROA. Given the tradeoff between solution time and accuracy, 500 tasks are distributed across all the logical cores. It consumes 1274.87 sec to obtain 500 invariant sets.

The SOSP approach in [18] is selected as a benchmark method due to its proven high performance on similar testing systems. The proposed data-driven method is compared with this approach in terms of computational performance and solution accuracy. To apply the SOSP, some simplifications are made to the system model (20). Firstly, the solar PV and the BESS are represented by a generic second-order model [50]. Secondly, the EV charging load is modeled as a CPL which can be further reduced as a controlled current source without internal dynamics [18]. Moreover, Taylor series expansion is utilized to recast the reduced-order model into a polynomial system because it contains rational equations. As in [18], the scaled-diagonally-dominant sums-of-squares programming (SDSOSP) [51] is also leveraged in lieu of the conventional SOSP for reduced solution time and improved scalability. The degree of the polynomial Lyapunov candidate function is selected as 4, while the degree of the truncated Taylor expansion is chosen as 3. In addition, the SPOT Toolbox and the MOSEK solver are used to solve the SDSOSP in MATLAB.

For different research focuses, the state variables of interest can be selected from the 21 system states for analysis. In this study, the transient frequency and voltage stabilities where the Ultra-Fast Charging Load (1) is to be connected are of interest. The estimated ROAs are respectively presented in a 2-dimensional plane with the other state variables set equal to zero, i.e., $v_{evdc,1}$ versus $i_{line,ev,1}$ and ω versus v_{bdc}. The solution accuracy of the proposed method and the SDSOSP is compared in Figs. 8 and 9, wherein the red star represents the projection of $\boldsymbol{x}_0$ and the blue square stands for the $\boldsymbol{x}_{eq}$. The blue dashed line delineates the boundary of the ROA estimated by the SDSOSP, while each green solid line encloses an invariant sublevel set of our linearly parameterized Lyapunov functions.

Both figures show that $\boldsymbol{x}_0$ lies in the estimated ROAs of $\boldsymbol{x}_{eq}$, indicating a large transient stability margin for the EDN. However, the proposed data-driven approach achieves a better ROA estimation than the SDSOSP. The reason is twofold. First, the linearly parameterized Lyapunov candidate functions have a degree of 8, while the polynomial Lyapunov candidate function only has a degree of 4. Second, a forward invariant subset of the actual ROA is enlarged when the maximum of the corresponding LP objective function is positive. Besides, it can be observed that some of the obtained forward invariant subsets are quite small and may also coincide. Nonetheless, through an increasing number of samplings, the proposed method significantly lessens the conservativeness of the ROA estimation.

A numerical simulation is conducted to further validate the obtained estimation. The power level at the Ultra-Fast Charging Load (1) is increased to 1600 kW to mimic the connection of

another two EV charging ports at t = 11.6 sec. Fig. 10 presents the transient response of the state variables of interest. After the EV charging load is increased, the DC-link voltages stabilize to new equilibria very soon, as shown in Fig. 10 (a). In contrast, Fig. 10 (b) shows that the angular frequency of the AC grid settles down after a longer transient period. This results from the difference in time scales between electromechanical and electromagnetic dynamics.

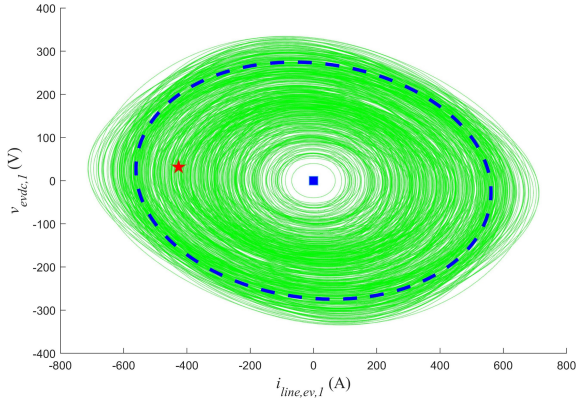

Fig. 8. Comparison of estimated ROAs ($v_{evdc,1}$ vs. $i_{line,ev,1}$).

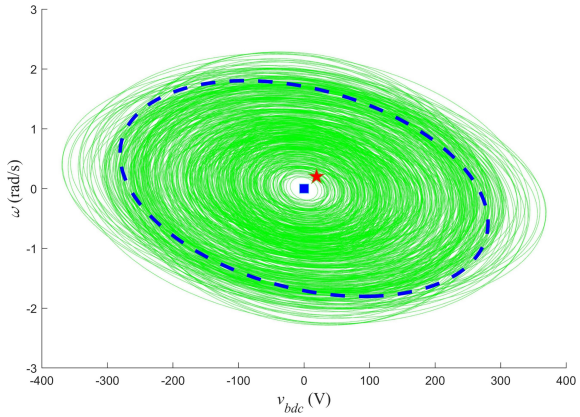

Fig. 9. Comparison of estimated ROAs (ω vs. v_{bdc}).

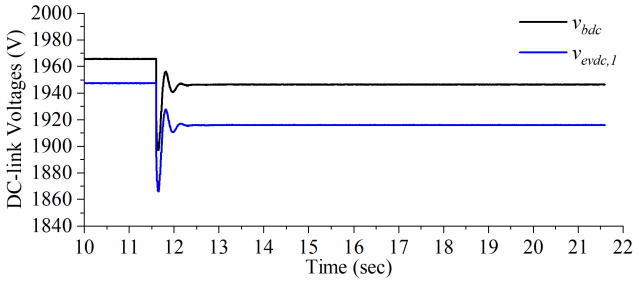

(a)

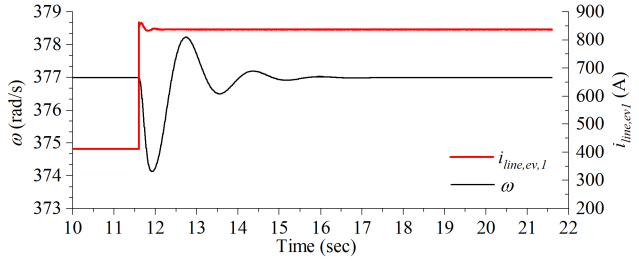

(b)

Fig. 10. Transient response of states after EV load increases.

Since the learning of Koopman eigenfunctions using the SOC algorithm can be implemented offline, the solution time of the proposed method is primarily determined by the ROA estimation based on sampling and LP. In the above case, it takes the SDSOSP as much as 5260.44 sec to obtain the estimates, in contrast to 1274.87 sec by the proposed method. To further explore the scalability, the DC EDN is expanded to include three and four EV charging loads, resulting in a system order increase of four and eight for the original EDN model (20), and two and four for the reduced EDN model, respectively. With all other settings unchanged, the computation times of the two methods for all these cases are reported in Table III.

TABLE III
COMPARISON OF COMPUTATION TIMES IN DIFFERENT CASES

# of EV Loads	**SDSOSP**	**Proposed Method**	
		SOC	**ROA Estimation**
2	5260.44	791.18	1274.87
3	38402.16	3821.67	4385.69
4	~	14889.72	27297.45

Time is in sec.

The results show that the computation time of the SDSOSP method substantially increases as the system scale increases. In the case where the number of EV loads reaches four, this method even fails to produce a solution within two days. In contrast, the proposed data-driven method is more scalable and consumes considerably less computation time to estimate the ROA. Furthermore, the proposed method consistently produced less conservative ROA estimation than the SDSOSP in all cases. Thus, the proposed method has the potential to facilitate real-time TSE.

VI. CONCLUSION AND FUTURE WORK

This paper proposed a Koopman-operator-based data-driven approach to estimate the ROA of a future DC EDN dominated by EV supercharging stations. Simulation results demonstrated that a less conservative ROA estimation could be obtained in a more computationally efficient manner, compared with the SOSP-based method (SDSOSP). With that, the proposed ROA estimation provides a possibility of real-time applications in future EDN TSE. In addition, the method is generic and could be readily applied to other dynamical systems if measured data are readily available. Further improving computational efficiency for larger-scale systems would be one of our future research directions. Multiple EV chargers can be integrated using aggregators, and modular DNNs can also be used to increase scalability. Apart from predicting the system's new equilibria in a purely data-driven fashion, we also plan on leveraging the control-Lyapunov functions to adaptively enlarge the estimated ROAs along with optimized dynamic EV charging.

APPENDIX

Prove that the family of sets $\boldsymbol{\mathcal{V}}_\gamma = \left\{\boldsymbol{x} \in \boldsymbol{\mathcal{R}}^p : \sum_{i=1}^{N_\phi} \alpha_i \cdot \phi_i(\boldsymbol{x}) \le \gamma\right\}$ with $\alpha_i > 0$ are forward invariant.

Proof:

According to the spectral property of the Koopman operator in [42], an eigenfunction $\varphi(\boldsymbol{x})$ and its corresponding eigenvalue $\lambda \in \boldsymbol{\mathcal{C}}$ of the Koopman operator $\boldsymbol{K}^t$ satisfies

$$\boldsymbol{K}^t \varphi(\boldsymbol{x}) = e^{\lambda t} \cdot \varphi(\boldsymbol{x})$$
$$\frac{d\varphi(\boldsymbol{x})}{dt} = \lambda \cdot \varphi(\boldsymbol{x})$$

For each $\phi_i(\boldsymbol{x}) \coloneqq \varphi_i(\boldsymbol{x}) \cdot \bar{\varphi}_i(\boldsymbol{x}) = |\varphi_i(\boldsymbol{x})|^2$ ($i = 1, 2, \dots, N_\phi$),

$$\dot{\phi}_i(\boldsymbol{x}) = \frac{d\phi_i(\boldsymbol{x})}{dt} = \frac{d\varphi_i(\boldsymbol{x})}{dt} \cdot \bar{\varphi}_i(\boldsymbol{x}) + \varphi_i(\boldsymbol{x}) \cdot \frac{d\bar{\varphi}_i(\boldsymbol{x})}{dt}$$

Note $\frac{d\bar{\varphi}_i(\boldsymbol{x})}{dt} = \overline{\frac{d\varphi_i(\boldsymbol{x})}{dt}} = \overline{\lambda_\iota \cdot \varphi_\iota(\boldsymbol{x})} = \bar{\lambda}_\iota \cdot \overline{\varphi_\iota(\boldsymbol{x})}$, thus

$$\dot{\phi}_i(\boldsymbol{x}) = \left(\lambda_i + \bar{\lambda}_i\right) \cdot |\varphi_i(\boldsymbol{x})|^2 = 2 \cdot \mathrm{Re}[\lambda_i] \cdot \phi_i(\boldsymbol{x})$$

Since the Koopman eigenfunctions are approximated using the SoC algorithm, there are approximation errors $\mathrm{e}_i(\boldsymbol{x})$'s. With a mild assumption that the errors are bounded such that $|\mathrm{e}_i(\boldsymbol{x})| \le \zeta_i \cdot \phi_i^2(\boldsymbol{x}) + \eta_i$ for some positive constants ζ_i and η_i,

$$\begin{aligned}\dot{\phi}_i(\boldsymbol{x}) &= 2 \cdot \mathrm{Re}[\lambda_i] \cdot \phi_i(\boldsymbol{x}) + \mathrm{e}_i(\boldsymbol{x}) \\ &\le 2 \cdot \mathrm{Re}[\lambda_i] \cdot \phi_i(\boldsymbol{x}) + |\mathrm{e}_i(\boldsymbol{x})| \\ &= \zeta_i \cdot \phi_i^2(\boldsymbol{x}) + 2 \cdot \mathrm{Re}[\lambda_i] \cdot \phi_i(\boldsymbol{x}) + \eta_i\end{aligned}$$

If $\dot{\phi}_i(\boldsymbol{x}) \le 0$ always holds for certain interval $(\underline{\gamma_i}, \overline{\gamma_i}) \subset \boldsymbol{\mathcal{R}}_{>0}$, the minimum of the above quadratic function of $\phi_i(\boldsymbol{x})$ should be negative, which leads to the condition $(\mathrm{Re}[\lambda_i])^2 > \zeta_i \cdot \eta_i$. It also implies that the $\overline{\gamma_i}$-sublevel set of $\phi_i(\boldsymbol{x})$ is forward invariant.

Furthermore, define $\gamma \coloneqq \min_i(\alpha_i \cdot \overline{\gamma_i})$ for $\alpha_i > 0$ ($i = 1, 2, \dots, N_\phi$). From $\sum_{i=1}^{N_\phi} \alpha_i \cdot \phi_i(\boldsymbol{x}) \le \gamma$, we have

$$\alpha_i \cdot \phi_i(\boldsymbol{x}) \le \gamma = \min_i(\alpha_i \cdot \overline{\gamma_i})$$

Thus, $\phi_i(\boldsymbol{x}) \le \overline{\gamma_i}$ holds for $i = 1, 2, \dots, N_\phi$.

Now, define $\beta \coloneqq 2 \cdot \min_i |\mathrm{Re}[\lambda_i]|$. Then,

$$\begin{aligned}\sum_{i=1}^{N_\phi} \alpha_i \cdot \dot{\phi}_i(\boldsymbol{x}) &\le \sum_{i=1}^{N_\phi} \alpha_i \cdot (2 \cdot \mathrm{Re}[\lambda_i]) \cdot \phi_i(\boldsymbol{x}) \\ &\quad + \sum_{i=1}^{N_\phi} \alpha_i \cdot [\zeta_i \cdot \phi_i^2(\boldsymbol{x}) + \eta_i] \\ &\le \sum_{i=1}^{N_\phi} \alpha_i \cdot (-\beta) \cdot \phi_i(\boldsymbol{x}) + \sum_{i=1}^{N_\phi} \alpha_i \cdot (\zeta_i \cdot \overline{\gamma_i}^2 + \eta_i)\end{aligned}$$

Therefore, if $\gamma \cdot \beta \ge \sum_{i=1}^{N_\phi} \alpha_i \cdot (\zeta_i \cdot \overline{\gamma_i}^2 + \eta_i)$,

$$\begin{aligned}\sum_{i=1}^{N_\phi} \alpha_i \cdot \dot{\phi}_i(\boldsymbol{x}) &\le \sum_{i=1}^{N_\phi} \alpha_i \cdot (-\beta) \cdot \phi_i(\boldsymbol{x}) + \gamma \cdot \beta \\ &= \beta \cdot [\gamma - \sum_{i=1}^{N_\phi} \alpha_i \cdot \phi_i(\boldsymbol{x})]\end{aligned}$$

This suggests that the γ-sublevel set of $\sum_{i=1}^{N_\phi} \alpha_i \cdot \phi_i(\boldsymbol{x})$ is forward invariant. It should also be noted that the condition $\gamma \cdot \beta \ge \sum_{i=1}^{N_\phi} \alpha_i \cdot (\zeta_i \cdot \overline{\gamma_i}^2 + \eta_i)$ can be easily met if β is large enough, which translates to that all λ_i's ($i = 1, 2, \dots, N_\phi$) have a sufficiently large negative real part.

Q.E.D.

REFERENCES

[1] U.S. EPA. (2022, Apr. 14). Sources of Greenhouse Gas Emissions. [Online]. Available: https://www.epa.gov/ghgemissions

[2] NJBPU. (2020, Jan. 27). 2019 New Jersey Energy Master Plan. [Online]. Available: https://nj.gov/emp/docs/pdf/2020_NJBPU_EMP.pdf

[3] M. Safayatullah, M. T. Elrais, S. Ghosh, R. Rezaii, and I. Batarseh, "A comprehensive review of power converter topologies and control methods for electric vehicle fast charging applications," *IEEE Access*, vol. 10, pp. 40753-40793, 2022.

[4] A. Emadi, A. Khaligh, C. H. Rivetta, and G. A. Williamson, "Constant power loads and negative impedance instability in automotive systems: Definition, modeling, stability, and control of power electronic converters and motor drives," *IEEE Trans. Veh. Technol*., vol. 55, no. 4, pp. 1112-1125, Jul. 2006.

[5] T. L. Vu and K. Turitsyn, "Lyapunov functions family approach to transient stability assessment," *IEEE Trans. Power Syst*., vol. 31, no. 2, pp. 1269-1277, Mar. 2016.

[6] T. Huang, S. Gao, and L. Xie, "A neural Lyapunov approach to transient stability assessment of power electronics-interfaced networked microgrids," *IEEE Trans. Smart Grid*, vol. 13, no. 1, pp. 106-118, Jan. 2022.

[7] H. K. Khalil, *Nonlinear Systems,* 3rd ed. Upper Saddle River, NJ, USA: Prentice Hall, 2002, pp. 312-322.

[8] M. Takagi and M. Sugeno, "Fuzzy identification of systems and its application to modeling and control," *IEEE Trans. Syst., Man, Cybern*., vol. SMC-15, no. 1, pp. 116-132, Feb. 1985.

[9] P. Magne, D. Marx, B. Nahid-Mobarakeh, and S. Pierfederici, "Large signal stabilization of a dc-link supplying a constant power load using a virtual capacitor: Impact on the domain of attraction," *IEEE Trans. Ind. Appl*., vol. 48, no. 3, pp. 878-887, May/Jun. 2012.

[10] M. Kabalan, P. Singh, and D. Niebur, "Nonlinear Lyapunov stability analysis of seven models of a DC/AC droop controlled inverter connected to an infinite bus," *IEEE Trans. Smart Grid*, vol. 10, no. 1, pp. 772-781, Jan. 2019.

[11] Y. Du, Y. Men, L. Ding, and X. Lu, "Large-signal stability analysis for inverter-based dynamic microgrids reconfiguration," *IEEE Trans. Smart Grid*, vol. 14, no. 2, pp. 836-852, March 2023.

[12] J. Grainger and W. Stevenson, Jr., *Power System Analysis*. New York, NY, USA: McGraw-Hill, 1994, pp. 271-274.

[13] Z. Li, W. Pei, H. Ye, and L. Kong, "Large signal stability analysis for DC microgrid under droop control based on mixed potential theory," *The J. Eng*., vol. 2019, no. 16, pp. 1189-1193, Mar. 2019.

[14] F. Chang, X. Cui, M. Wang, and W. Su, ''Region of attraction estimation for DC microgrids with constant power loads using potential theory,'' *IEEE Trans. Smart Grid*, vol. 12, no. 5, pp. 3793-3808, Sep. 2021.

[15] S. Izumi, H. Somekawa, X. Xin, and T. Yamasaki, "Estimation of regions of attraction of power systems by using sum of squares programming," *Electr Eng*, 100, pp. 2205-2216, 2018.

[16] L. Kalemba, K. Uhlen, and M. Hovd, "Stability assessment of power systems based on a robust sum-of-squares optimization approach," *2018 Power Systems Computation Conference (PSCC)*, Dublin, Ireland, 2018, pp. 1-8.
[17] Z. Zhang, R. Schuerhuber, L. Fickert, F. Katrin, G. Chen, and Y. Zhang, "Domain of attraction's estimation for grid connected converters with phase-locked loop," *IEEE Trans. Power Syst*., vol. 37, no. 2, pp. 1351-1362, Mar. 2022.
[18] B. Severino and K. Strunz, "Enhancing transient stability of DC microgrid by enlarging the region of attraction through nonlinear polynomial droop control," *IEEE Trans. Circuits Syst. I, Reg. Papers*, vol. 66, no. 11, pp. 4388-4401, Nov. 2019.
[19] Y. Xia, W. Wei, T. Long, F. Blaabjerg, and P. Wang, "New analysis framework for transient stability evaluation of DC microgrids," *IEEE Trans. Smart Grid*, vol. 11, no. 4, pp. 2794-2804, Jul. 2020.
[20] I. Mezić, "Koopman operator, geometry, and learning," doi: https://doi.org/10.1090/noti2306.
[21] C. Josz, D. K. Molzahn, M. Tacchi, and S. Sojoudi, "Transient stability analysis of power systems via occupation measures," in *Proc. IEEE Conf. Innov. Smart Grid Technol*., Washington, DC, USA, Feb. 2019, pp. 1-5.
[22] S. L. Brunton and J. N. Kutz, *Data-Driven Science and Engineering: Machine Learning, Dynamical Systems, and Control*. Cambridge, UK: Cambridge University Press, 2019, pp. 229-235.
[23] M. Netto and L. Mili, "A robust data-driven Koopman Kalman filter for power systems dynamic state estimation," *IEEE Trans. Power Syst*., vol. 33, no. 6, pp. 7228-7237, 2018.
[24] L. Guo, Y. Zhang, X. Li, *et al*., "Data-driven power flow calculation method: a lifting dimension linear regression approach," *IEEE Trans. Power Syst*., vol. 37, no. 3, pp. 1798-1808, May 2022.
[25] P. Sharma, V. Ajjarapu, and U. Vaidya, "Data-driven identification of nonlinear power system dynamics using output-only measurements," *IEEE Trans. Power Syst*., vol. 37, no. 5, pp. 3458-3468, Sept. 2022.
[26] A. Husham, I. Kamwa, M. A. Abido, and H. Suprême, "Decentralized stability enhancement of DFIG-based wind farms in large power systems: Koopman theoretic approach," *IEEE Access*, vol. 10, pp. 27684-27697, 2022.
[27] A. Mauroy and I. Mezić, "Global stability analysis using the eigenfunctions of the Koopman operator," *IEEE Trans. Autom. Control*, vol. 61, no. 11, pp. 3356-3369, Nov. 2016.
[28] Y. Susuki and I. Mezić, "Nonlinear Koopman modes and power system stability assessment without models," *IEEE Trans. Power Syst*., vol. 29, no. 2, pp. 899-907, Mar. 2014.
[29] Y. Hirase, Y. Ohara, N. Matsuura, and T. Yamazaki. "Dynamics analysis using Koopman mode decomposition of a microgrid including virtual synchronous generator-based inverters," *Energies*, vol. 14, no. 15, p. 4581, 2021.
[30] H. Choi and S. Bose, "Transient stability analysis of power systems using Koopman operators," preprint, 2018. [Online]. Available: https://boses.ece.illinois.edu/files/TSKoopman.pdf
[31] M. O. Williams, I. G. Kevrekidis, and C. W. Rowley. "A data–driven approximation of the Koopman operator: extending dynamic mode decomposition," *J Nonlinear Sci* 25, pp. 1307-1346, 2015.
[32] M. Han, J. Euler-Rolle, and R. K. Katzschmann, "DeSKO: stability-assured robust control with a deep stochastic Koopman operator," in *Proc. ICLR 2022,* Virtual, Apr. 25, 2022.
[33] G. Mamakoukas, O. Xherija, and T. D. Murphey, "Memory-efficient learning of stable linear dynamical systems for prediction and control," in *Proc. NeurIPS 2020,* Virtual, Dec. 6-12, 2020.
[34] N. Gillis, M. Karow, and P. Sharma, "Approximating the nearest stable discrete-time system," *Linear Algebra Appl*, vol. 573, no. 15, pp. 37-53, Jul. 2019.
[35] J. J. Justo, F. Mwasilu, J. Lee, J. W. Jung, "AC-microgrids versus DC-microgrids with distributed energy resources: A review," *Renew. Sust. Energ. Rev.*, vol. 24, pp. 387-405, Aug. 2013.
[36] T. Ma, H. Yang, and L. Lu, "Solar photovoltaic system modeling and performance prediction," *Renew. Sust. Energ. Rev.*, vol. 36, pp. 304-315, Aug. 2014.
[37] A. Sangwongwanich, Y. Yang, F. Blaabjerg, and H. Wang, "Benchmarking of constant power generation strategies for single-phase grid-connected photovoltaic systems," *IEEE Trans. Ind. Appl.*, vol. 54, no. 1, pp. 447-457, Jan. 2018.
[38] M. Akil, E. Dokur, and R. Bayindir, "The SOC based dynamic charging coordination of EVs in the PV-penetrated distribution network using real-world data," *Energies*, vol. 14, no. 24, p. 8508, 2021.
[39] O. Tremblay, L.A. Dessaint, and A.I. Dekkiche, "A generic battery model for the dynamic simulation of hybrid electric vehicles," in *Proc. IEEE Vehicle Power Propuls. Conf. (VPPC)*, Sep. 2007, pp. 284-289.
[40] R. Teodorescu, M. Liserre, and P. Rodriguez, *Grid Converters for Photovoltaic and Wind Power Systems*. West Sussex, UK: IEEE Wiley, 2011, pp. 317-320.
[41] J. H. Chow, M. A. Pai, and P. W. Sauer, *Power system dynamics and stability, 2nd ed.* Hoboken, NJ, USA: IEEE Wiley, 2018.
[42] A. Mauroy, I. Mezić, and Y. Susuki, *The Koopman Operator in Systems and Control*. Switzerland: Springer Nature, 2020.
[43] D. M. Mount, (Fall 2016). *Computational Geometry*. [Online]. Available: https://www.cs.umd.edu/class/fall2016/cmsc754/Lects/cmsc754-fall16-lects.pdf
[44] B. Cousins, "Efficient high-dimensional sampling and integration," Ph.D. dissertation, Coll. Comp., Tech. GT, Atlanta, GA, USA, 2017.
[45] S. Bacha, I. Munteanu, and A. I. Bratcu, *Power Electronic Converters Modeling and Control with Case Studies*. London, UK: Springer-Verlag, 2014, pp. 55-71.
[46] L. Yao, W. H. Lim, and T. S. Tsai, "A real-time charging scheme for demand response in electric vehicle parking station," *IEEE Trans. Smart Grid*, vol. 8, no. 1, pp. 52-62, Jan. 2017.
[47] P. Sarajcev, A. Kunac, G. Petrovic, and M. Despalatovic, "Artificial intelligence techniques for power system transient stability assessment," *Energies*, vol. 15, no. 2, p. 507, 2022.
[48] A. Geron, *Hands-On Machine Learning with Scikit-Learn, Keras, and TensorFlow: Concepts, Tools, and Techniques to Build Intelligent Systems*. Sebastopol, CA, USA: O'Reilly Media, 2022.
[49] I. Nayak, M. Kumar, and F. L. Teixeira, "Detection and prediction of equilibrium states in kinetic plasma simulations via mode tracking using reduced-order dynamic mode decomposition," *J. Comput. Phys.*, vol. 447, Dec. 2021.
[50] M. A. Mahmud, T. K. Roy, S. Saha, M. E. Haque, and H. R. Pota, "Robust nonlinear adaptive feedback linearizing decentralized controller design for islanded DC microgrids," *IEEE Trans. Ind. Appl*., vol. 55, no. 5, pp. 5343-5352, Sep. 2019.
[51] A. A. Ahmadi and A. Majumdar, "DSOS and SDSOS optimization: More tractable alternatives to sum of squares and semidefinite optimization," *SIAM J. Appl. Algebra Geometry*, vol. 3, no. 2, pp. 193-230, Apr. 2019.

Jimiao Zhang (GSM'18, M'23) received his B.Eng. degree in Computer Engineering and M.Eng. degree in Electric Engineering from Guangdong University of Foreign Studies and Chongqing University, China, in 2012 and 2015, respectively. He earned his Ph.D. in Electrical and Computer Engineering from Rowan University, New Jersey, USA, in 2023. He is currently a research associate in the Electrical and Computer Engineering Department, Rowan University. From 2015 to 2017, he worked as a Transmission Line Engineer for the State Grid Chongqing Electric Power Company. His research interests include operation and control of electrical distribution systems, renewable energy generation and integration.

Jie Li (M'14) received the B.S. degree in information engineering from Xi'an Jiaotong University in 2003 and the M.S. degree in system engineering from Xi'an Jiaotong University, China in 2006, and the Ph.D. degree from the Illinois Institute of Technology (IIT), Chicago, in 2012. From 2006 to 2008, she was a Research Engineer with IBM China Research Lab. From 2012 to 2013, she was a Power System Application Engineer with GE Energy Consulting. She was an Assistant Professor with the Electrical and Computer Engineering Department, Clarkson University, Potsdam, NY, USA, during 2014 to 2019. She is currently an Associate Professor with the Electrical and Computer Engineering Department, Rowan University, Glassboro, NJ, USA. Her research interests include power systems planning, operation, and control.